Supplementary Information:

Linear-polarized Terahertz Isolator by Breaking the Gyro-Mirror Symmetry in Cascaded Magneto-Optical Metagrating

Zhiyu Tan¹, Fei Fan^{1*}, Dan Zhao², Shanshan Li¹, Xianghui Wang¹, Shengjiang Chang²

- S1. THE MAGNETO-OPTICAL PROPERTIES FOR THE INSB
- **S2. EXPERIMENT SETUP**
- S3. ELLIPTICITY AND OPTICAL ROTATION ANGLE
- **S4. SIMULATION METHOD AND SIMULATION RESULTS**

¹ Institute of Modern Optics, Nankai University, Tianjin Key Laboratory of Micro-scale Optical Information Science and Technology, Tianjin 300350, China

² Tianjin Key Laboratory of Optoelectronic Sensor and Sensing Network Technology, Tianjin 300350, China

^{*}Corresponding author: <u>fanfei@nankai.edu.cn</u>

S1. THE MAGNETO-OPTICAL CHIRALITY FOR THE INSB

In Eq. 1 in the main text, the dielectric tensor elements ε_1 and ε_2 follow the Drude-Lorentz model that can be written as follows:

$$\varepsilon_{1} = \varepsilon_{\infty} - \frac{\omega_{p}^{2}(\omega + \gamma i)}{\omega[(\omega + \gamma i)^{2} - \omega_{c}^{2}]}$$

$$\varepsilon_{2} = -\frac{\omega_{p}^{2}\omega_{c}}{\omega[(\omega + \gamma i)^{2} - \omega_{c}^{2}]}$$
(S1)

where $\varepsilon_{\infty} = 15.68$ is the high-frequency limit permittivity; ω is the circular frequency of the incident THz wave; ω_p is plasma frequency written as $\omega_p = (Ne^2/m^*\mu)^{1/2}$, N is carrier density, ε_0 is the free-space permittivity; γ is the collision frequency of carriers, $\gamma = e/(\mu m^*)$, and μ is the carrier mobility, which is a function of the temperature modeled as $\mu = 7.7 \times 10^4 \, (T/300)^{-1.66} \, \text{cm}^2 \cdot \text{V}^{-1} \cdot \text{s}^{-1}$. Moreover, the carrier density N the dielectric which depends on the temperature T. In this work, $N=4\times 10^{14} \, \text{cm}^{-3}$ at 80 K according to the experimental measurement. Then, we got the experiment results of the intensity transmittance of InSb with linear-polarized state incidence and without MF, as shown in Fig. S1(a). The spectrum shows that InSb has high pass filtering characteristics for THz broadband wave, and the cut-off frequency is near 0.4 THz. The cut-off frequency of the InSb is dependent on the plasma frequency, which means the cut-off frequency is dependent on the carrier density. Below this frequency, InSb is strongly lossy to THz wave, and above this frequency, InSb is highly transparent. In the high-frequency region of > 0.8THz, the lowest insertion loss of InSb is about 3dB.

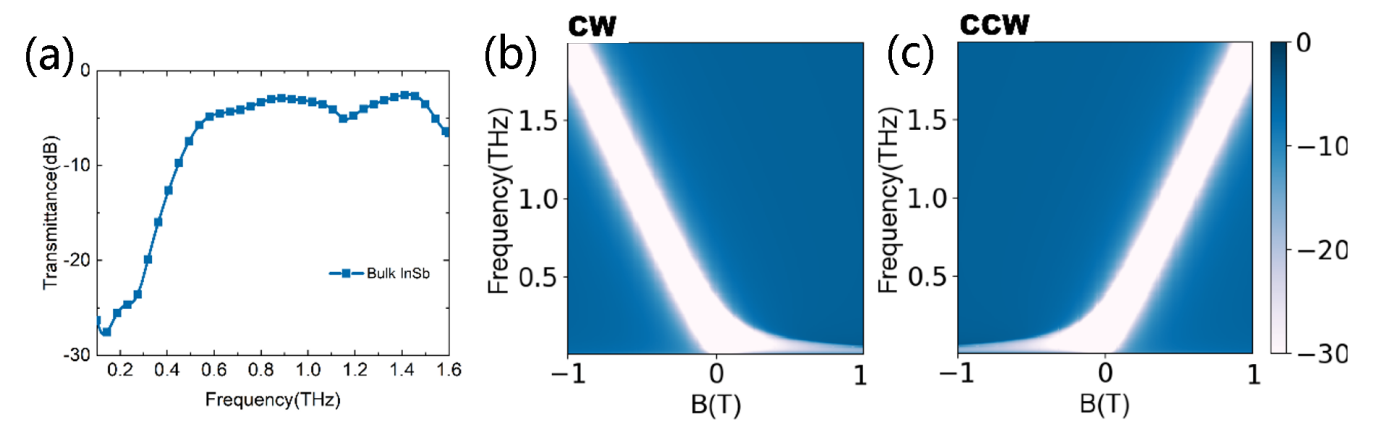


Fig. S1. (a) The experiment results for the transmittance of InSb for the linear-polarized state without the MF at 80 K. The calculated transmittance (in dB) of the 300µm thick InSb for the (b) CW and (c) CCW states.

From Eqs. (S1) and (3) in the main text, we can get the transmittance of the InSb for the circularly polarized (CP) light. Here, the thickness of the InSb is $d = 300 \, \mu m$. As shown in Fig. S1(b) and S1(c), the transmittance (in dB) maps for the clockwise (CW) and counter-clockwise (CCW) states are observed. It shows a strong gyro-mirror symmetry for these two orthogonal states: for the CW state with the growth of the positive MF, the forbidden region (the white region with the transmittance <-30dB) moves to the lower frequencies, but for the negative MF, the forbidden region moves to the higher frequencies. For a CW wave propagating backward, when the MF direction is unchanged relative to the absolute coordinate system, the MF has reversed relative to the backward propagation direction, which is equivalent to the result that the forward transmission with the negative MF in Fig. S1(b). Therefore, the longitudinally magnetized InSb shows the nonreciprocal one-way transmission for the CW or CCW state in the THz regime or called nonreciprocal circular dichroism. However, for the CCW state, the transmittance map is reversed with that of the CW state to the MF or propagation direction as shown in Fig. S1(c), showing the gyro-mirror symmetry.

S2. EXPERIMENT SETUP:

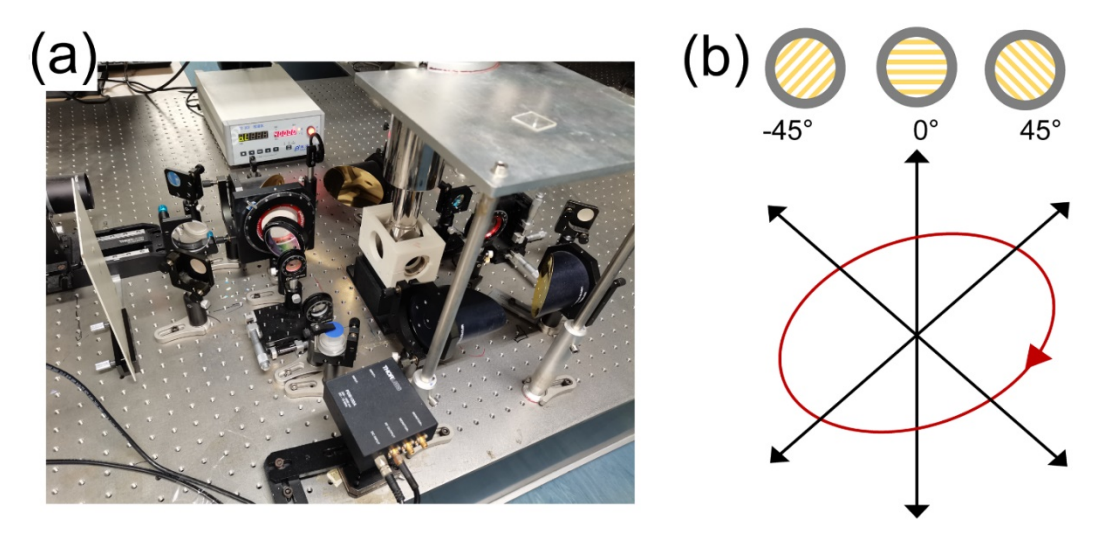


Fig. S2. (a) Photo of the THz-TDMPS system with the Dewar flask-sample cell and two THz metallic wire polarizers. (b) Illustration of arbitrary polarization ellipsoid reconstructed by a pair of detected orthogonal LP states.

In this work, we use the terahertz time-domain magneto polarization spectroscopy (THz-TDMPS) system for the experiment. The schematic view of the experiment system is shown in Fig. S2(a). The THz signal is generated by the photoconductive antenna with an 800nm femtosecond laser pumping. And in the receiver port, a (110) ZnTe crystal is used for the electro-optical detection probed by the y-direction linear polarized (LP) femtosecond laser. Therefore, the (001) axis of the ZnTe is rotated along the x-axis to get the best efficiency.

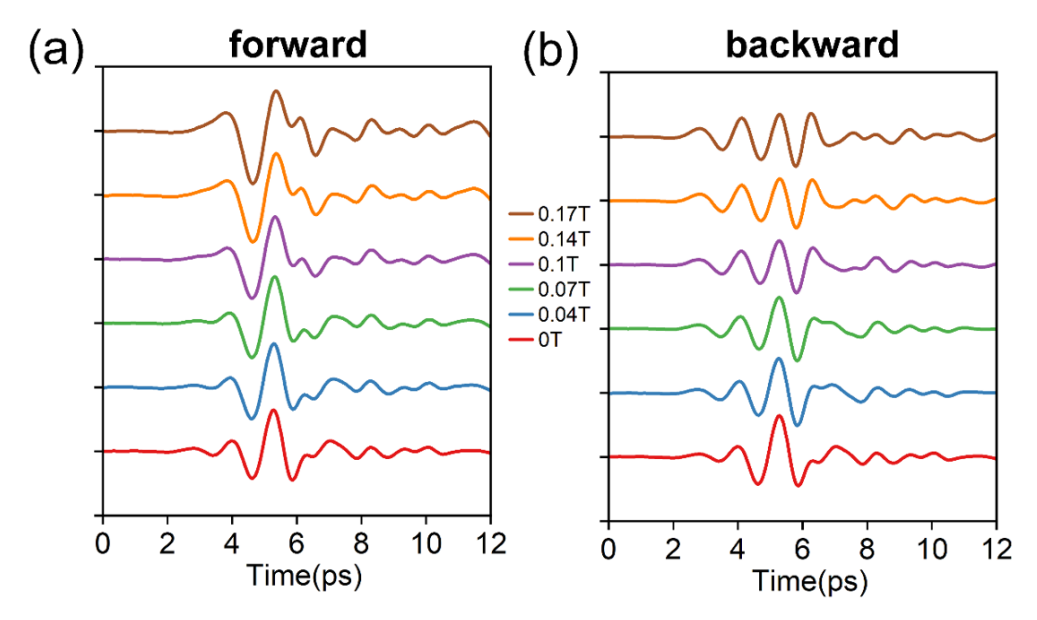


Fig. S3. (a) The time-domain signal of the y-LP under the forward MFs and (b) backward MFs.

Then, a couple of additional polarizers are placed both in front of and behind the sample to adjust the polarization states of both incident and received signal. The front side polarizer is fixed to 0° to ensure the incident light is y-polarized. And at the detector port, we can rotate the polarizer to obtain the signal of a specific polarized-LP state as shown in Fig. S2(b). When the second polarizer is rotated to 0°, we can obtain the LP time-domain pulse signal for the meta-grating/InSb/meta-grating (GIG) structure under different

 $\tilde{E}_s(f) = A_s(f)e^{i\theta}/|A_r(f)|$, where ~ denotes the variable is complex, subscript s denotes the

sample, and r denotes the reference data (Dewar flask without any object inside). Thus, the transmittance can be obtained as $T_s = \left|\tilde{E}_s(f)\right|^2$, which can be seen in Fig. 3 in the main text.

In addition, to confirm the complete polarization state of the output wave, we turn the second polarizer to $+45^{\circ}$ and -45° as shown in Fig. S2(b). We can therefore get the relative electric field intensity $\tilde{E}_{s\pm45}(f) = A_{s\pm45}(f)e^{i\theta_{245}}/|A_r(f)|$. The spin chiral components can be derived by:

$$\begin{pmatrix}
\tilde{E}_{CW} \\
\tilde{E}_{CCW}
\end{pmatrix} = \frac{1}{\sqrt{2}} \begin{pmatrix} 1 & i \\ 1 & -i \end{pmatrix} \begin{pmatrix} \tilde{E}_{s+45^{\circ}} \\ \tilde{E}_{s-45^{\circ}} \end{pmatrix},
\begin{pmatrix}
T_{CW} \\
T_{CCW}
\end{pmatrix} = \begin{pmatrix} \left|\tilde{E}_{CW}\right|^{2} \\ \left|\tilde{E}_{CCW}\right|^{2} \end{pmatrix}.$$
(S2)

S3. ELLIPTICITY AND OPTICAL ROTATION ANGLE:

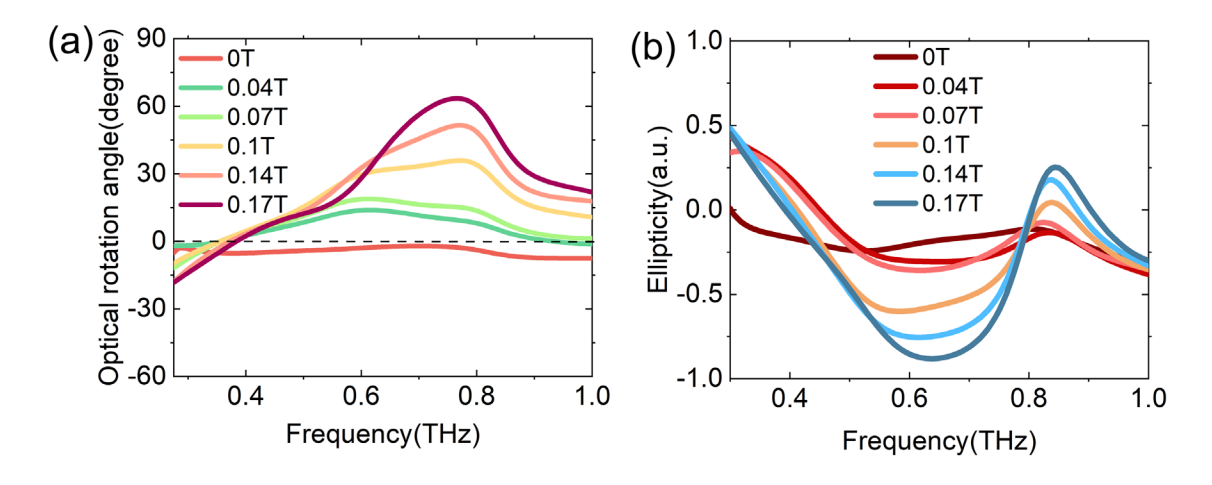


Fig. S4. (a) ORA and (b) ellipticity spectra of the GIG f under the different positive MFs.

We calculated the ellipticity and optical rotation angle to reflect the optical chiral state of the device. Here, we define the ellipticity (EP) and optical rotation angle (ORA) as:

$$EP = \frac{T_{CW} - T_{CCW}}{T_{CW} + T_{CCW}}$$
 (S3)

$$ORA = \frac{\arg(\tilde{E}_{CW}) - \arg(\tilde{E}_{CCW})}{2}$$
 (S4)

where T_{CW} and T_{CCW} are the intensity transmission, and the $\arg(\tilde{E}_{CW})$ and $\arg(\tilde{E}_{CCW})$ are the phase angle (in degree) of CW and CCW components. The ellipticity shows the polarization states of the output wave (e.g. when EP=1 indicates the CW output, EP=0 indicates the pure LP output).

In Fig. S4(a), the ellipticity for the forward MFs is obtained. For the forward MFs, when the frequency is around 0.42 THz and B = 0.17T, the ellipticity EP = 0, output purely LP state. Between 0.5-0.7 THz, with the growth of the MFs, the ellipticity decreases which means output CW-like states. The OA indicates the phase shift between two orthogonal CP states which also indicates the polarization angle of the output wave as shown in Fig. S4(b). Around 0.4THz, for the forward MFs, the ORA is closed to 0, which means the polarization direction is merely unchanged. At higher frequencies, with the growth of the MFs, the ORA shows the Faraday MO rotation effect for the forward and backward MFs.

In Fig. 4 in the main text, we also draw the polarization ellipse to fully represent the arbitrary polarization state of the output wave, also defined as the terminal trajectory equation of electric vector E, and the equation of the ellipse can be written as:

$$\left(\frac{x}{T_{-45^{\circ}}}\right)^{2} + \left(\frac{y}{T_{+45^{\circ}}}\right)^{2} - \frac{2xy}{T_{-45^{\circ}}T_{+45^{\circ}}}\cos\Delta\delta = \sin^{2}\Delta\delta$$
 (S5)

S4. SIMULATION METHOD AND SIMULATION RESULTS:

We simulated both the meta-gratings and the GIG structure by using the finite-difference time-domain (FDTD) method in the commercial software FDTD SOLUTION from Ansys Lumerical Enterprise. The grating-InSb-grating model is built according to the practically fabricated geometric structures, and the dispersion curves of the InSb dielectric tensor elements are fitted as the data obtained from the experimental tests and the theoretical parameters of InSb, and then imported into the simulation software as the simulation parameters.

For the simulation of the first GIG structure, we simulate a supercell with 13×2 units inside, and the boundary conditions for the x- and y- directions are set to periodic. We set a pair of orthogonal LP plane wave propagating with the z-axis. The phase difference between these two plane waves is +90° or -90° for the CW state and CCW state, respectively. As shown in Fig. S5(a), with the increase with the MFs, the transmittance for the forward wave is increasing, and decreasing for the backward wave, which well coincides with the experimental data as shown in Fig. 3(c) in the main text. We also simulated the electric field distribution of the first GIG structure for the forward and backward propagation at 0.4 THz under the MF of 0.17 T in Fig. S6, which shows the one-way transmission property of the device.

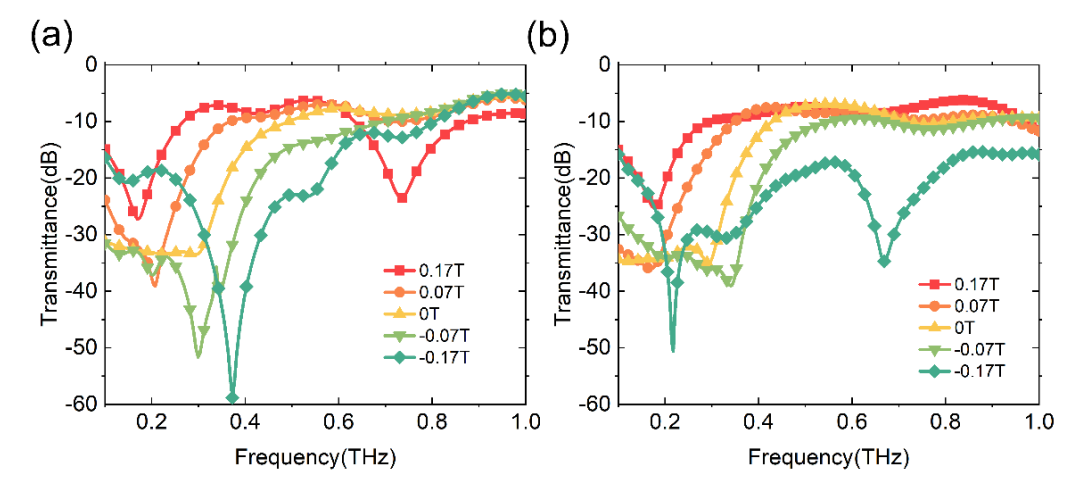


Fig. S5. The simulated transmittance for (a) the first GIG and the (b) the second broadband GIG structure under different MFs.

For the simulation of the second GIG structure with two perfect isolation points, we simulated a unit cell with a 200µm×200µm

period for the x-y plane. The boundary conditions and sources are set as the same as the first GIG structure. As shown in Fig. S5(b), with the growth of the MFs, the forward transmittance increasing and the backward transmittance decreasing, meanwhile, the isolation band broaden. For the MF B = 0.17T, there are also two perfect isolation points around 0.2 THz and 0.7 THz. These results are in agreement with the experimental results in Fig. 5(c) in the main text.

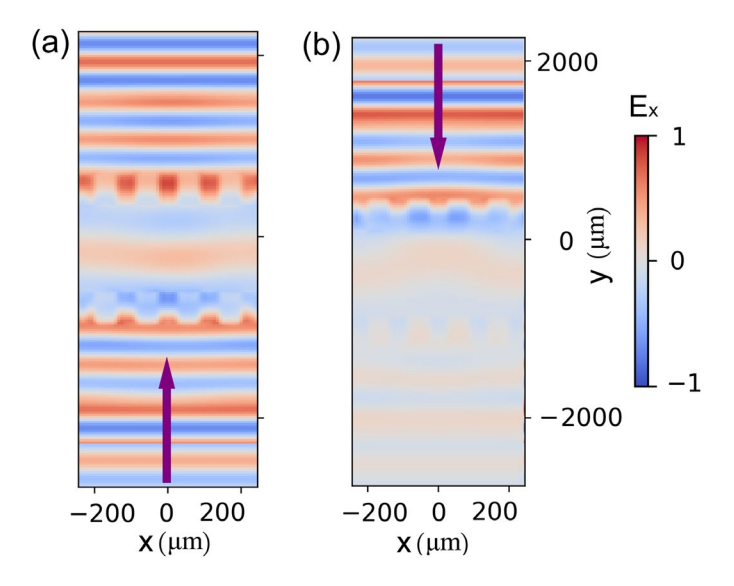


Fig. S6. The simulated electric field distribution of the first GIG structure for (a) forward propagation and (b) backward propagation at 0.4 THz under the MF of 0.17 T.